

Prediction of oxide phases formed upon internal oxidation of advanced high-strength steels

Mao, W.; Sloof, Willem G.; Hendrikx, Ruud W.A.

DOI

[10.1007/s11085-017-9815-4](https://doi.org/10.1007/s11085-017-9815-4)

Publication date

2017

Document Version

Final published version

Published in

Oxidation of Metals

Citation (APA)

Mao, W., Sloof, W. G., & Hendrikx, R. W. A. (2017). Prediction of oxide phases formed upon internal oxidation of advanced high-strength steels. *Oxidation of Metals*, 89 (June 2018)(5-6), 531-549. <https://doi.org/10.1007/s11085-017-9815-4>

Important note

To cite this publication, please use the final published version (if applicable). Please check the document version above.

Copyright

Other than for strictly personal use, it is not permitted to download, forward or distribute the text or part of it, without the consent of the author(s) and/or copyright holder(s), unless the work is under an open content license such as Creative Commons.

Takedown policy

Please contact us and provide details if you believe this document breaches copyrights. We will remove access to the work immediately and investigate your claim.

Prediction of Oxide Phases Formed upon Internal Oxidation of Advanced High-Strength Steels

Weichen Mao^{1,2} · Ruud W. A. Hendrikx² · Willem G. Sloof²

Received: 24 July 2017 / Revised: 16 October 2017
© The Author(s) 2017. This article is an open access publication

Abstract The effect of Cr on the oxidation of Fe–Mn-based steels during isothermal annealing at different dew points was investigated. The Fe–Mn–Cr–(Si) phase diagrams for oxidizing environments were computed to predict the oxide phases. Various Fe–Mn steels with different concentrations of Cr and Si were annealed at 950 °C in a gas mixture of Ar or N₂ with 5 vol% H₂ and dew points ranging from – 45 to 10 °C. The identified oxide species after annealing match with those predicted based on the phase diagrams. (Mn,Fe)O is the only oxide phase formed during annealing of Fe–Mn binary steel alloys. Adding Cr leads to the formation of (Mn,Cr,Fe)₃O₄ spinel. The dissociation oxygen partial pressure of (Mn,Cr,Fe)₃O₄ in the Fe–Mn–Cr steels is lower than that of (Mn,Fe)O. The Si in the steels results in the formation (Mn,Fe)₂SiO₄, and increasing the Si concentration suppresses the formation of (Mn,Cr,Fe)₃O₄ and (Mn,Fe)O during annealing.

Keywords Advanced high-strength steels · Annealing · Oxidation · Thermodynamics

Introduction

Advanced high-strength steels (AHSS) are widely used for automotive applications to reduce the weight of car bodies and thereby reducing fuel consumption and CO₂ emissions; see, for example, [1]. To protect AHSS against corrosion, a zinc coating is applied onto the steel surface usually by hot-dip galvanizing [2]. Before entering

✉ Weichen Mao
w.mao@tudelft.nl

¹ Materials innovation institute (M2i), Elektronicaweg 25, 2628 XG Delft, The Netherlands

² Department of Materials Science and Engineering, Delft University of Technology, Mekelweg 2, 2628 CD Delft, The Netherlands

the zinc bath the steel strip passes through continuous annealing furnaces. The annealing atmosphere is usually a gas mixture of N_2 and H_2 with dew points ranging from -60 to 10 °C, whose oxygen partial pressure level is below the dissociation oxygen partial pressure of Wüstite (FeO). However, the alloying elements (e.g. Mn, Cr, Si, Al) in AHSS have a higher affinity to oxygen than iron, leading to the formation of oxides of these elements during the annealing process prior to galvanizing. The presence of these alloying element oxides at the steel surface reduces the zinc wettability [3] and thus impairs the galvanizing quality [4]. Therefore, it is imperative to understand the oxidation behaviour of AHSS in N_2 plus H_2 gas mixtures with various dew points and to find conditions to mitigate the formation of external oxides after annealing.

The oxidation behaviour of Fe–Mn binary and Fe–Mn–Si ternary steel alloys below the dissociation oxygen partial pressure of FeO has been studied in detail (see, for example, Refs. [5–9]). However, only a few studies have been reported on the oxidation of Cr-alloyed Fe–Mn-based steels [10, 11]. The study on the effect of Cr on the type of oxides formed in AHSS during annealing is not complete, and the type of oxides formed during annealing of Fe–Mn–Cr ternary and Fe–Mn–Cr–Si quaternary steel alloys has not been confirmed by X-ray diffraction analysis. Since Cr is often added to AHSS to enhance the hardenability of austenite [1], the primary aim of the present investigation is to understand the effect of Cr on the type of oxides formed in Fe–Mn-based steels during annealing. Also, the effect of Si on the type of oxide species formed in steels alloyed with both Mn and Cr is studied. The type and composition of the oxides formed in Fe–Mn–Cr–(Si) steel alloys as a function of annealing temperature, alloy composition and the annealing dew points are first predicted with thermodynamic computation. Then, the experimentally identified oxide phases formed after annealing different Fe–Mn–Cr–(Si) steel alloys in gas mixtures of Ar or N_2 with 5 vol% H_2 and different dew points are compared with the thermodynamic predictions. Finally, the effect of Cr and Si on the internal and external oxidations of Fe–Mn-based steels is discussed.

Experimental Procedures

Samples

The chemical composition in atom per cent of the steel alloys investigated is listed in Table 1. The Fe–1.7Mn, Fe–1.8Mn–0.6Cr–0.5Si, Fe–1.8Mn–1.1Cr–0.5Si and Fe–2.8Mn–0.6Cr–0.5Si steel samples were cut with a plate cutter from a cold-rolled steel sheet. The Fe–1.8Mn–0.5Cr and Fe–1.7Mn–1.5Cr alloys were cut from ingots, and the Fe–1.9Mn–1.0Cr–0.1Si and Fe–1.9Mn–1.6Cr–0.1Si steels were cut from hot-rolled steel plates by electric discharge machining (EDM). Before annealing, the surface of specimens was ground with SiC emery paper and then polished with 1-micron diamond grains. Finally, the samples were cleaned ultrasonically in isopropanol and dried by blowing with pure nitrogen (purity better than 5 N). The samples were stored in air-tight membrane boxes (Agar Scientific G3319, the UK).

Table 1 Steel composition in atom per cent (weight per cent in parentheses)

Sample	C	Mn	Cr	Si	Al
Fe–1.7Mn	0.48 (0.10)	1.72 (1.70)	–	0.10 (0.05)	0.004 (0.002)
Fe–1.8Mn–0.5Cr	–	1.75 (1.72)	0.53 (0.49)	–	–
Fe–1.7Mn–1.5Cr	–	1.70 (1.67)	1.49 (1.39)	–	–
Fe–1.8Mn–0.6Cr–0.5Si	0.46 (0.10)	1.82 (1.80)	0.57 (0.53)	0.49 (0.25)	0.006 (0.003)
Fe–1.8Mn–1.1Cr–0.5Si	0.47 (0.10)	1.82 (1.80)	1.09 (1.02)	0.51 (0.26)	0.039 (0.019)
Fe–1.9Mn–1.0Cr–0.1Si	0.46 (0.10)	1.90 (1.88)	0.97 (0.91)	0.12 (0.06)	0.053 (0.026)
Fe–1.9Mn–1.6Cr–0.1Si	0.46 (0.10)	1.85 (1.83)	1.63 (1.53)	0.10 (0.05)	0.049 (0.024)
Fe–2.8Mn–0.6Cr–0.5Si	0.47 (0.10)	2.83 (2.80)	0.59 (0.55)	0.49 (0.25)	0.010 (0.005)

Annealing

The oxidation experiments below the dissociation oxygen partial pressure of Wüstite were carried out in a horizontal quartz tube furnace (Carbolite MTF 12/38/850, the UK) with an inner tube diameter of 30 mm. The temperature in the furnace tube was measured with a NiCr/NiAl (type K) thermocouple at the sample location. A gas mixture of N₂ or Ar with 5 vol% H₂ was passed through the furnace tube at atmospheric pressure. De-aerated and deionized water (18.2 MΩ cm at 25 °C) was evaporated with a controlled evaporator mixer (CEM, Bronkhorst, the Netherlands) to create specific dew points of – 45, – 37, – 30, – 10 and 10 °C (corresponding oxygen partial pressures of 8.1×10^{-22} , 5.0×10^{-21} , 2.2×10^{-20} , 1.0×10^{-18} and 2.3×10^{-17} atm. at 950 °C; see “Appendix”) in the furnace. The pure water was de-aerated with nitrogen gas in a closed pressurized stainless steel vessel, and the dissolved oxygen gas in the pure water was below 100 ppb, as measured with an O₂ sensor (InPro 6850i, Mettler Toledo, the USA). The dew points of – 10 and 10 °C were monitored with a cooled mirror analyser (Optidew, Michell Instruments, the UK). The dew points of – 45, – 37 and – 30 °C were monitored with another cooled mirror analyser (S4000 TRS, Michell Instruments, the UK). The fluctuation of dew points during annealing was within ± 2 °C. The partial pressure of evaporated H₂O in the gas mixture is related to dew point according to the formula given in “Appendix”. The gas mixture with dew points of – 10 and 10 °C consists of N₂ + 5 vol% H₂, while the gas mixture with dew points of – 45, – 37 and – 30 °C was created with Ar + 5 vol% H₂. However, the oxidation behaviour of the steel alloys used in this study is not affected by the type of carrier gas (i.e. Ar or N₂), because formation of nitride is not thermodynamically favourable for our samples and our annealing conditions. The flow rate of gas mixture with dew points of – 30 to 10 °C was 1500 sccm, while the flow rate of gas mixture with dew points of – 45 and – 37 °C was 3000 sccm. Before annealing, the sample was placed onto a quartz boat located at the cold zone of the furnace tube. Then, the furnace was closed and flushed with the reaction gas for more than 30 min. Next, the sample was moved to the hot zone of the furnace with a quartz rod to start an annealing cycle. At the end of the annealing cycle, the sample was moved in the reverse direction, i.e. to the

cold zone. The heating and cooling of the sample were relatively fast, about 140 and 180 °C/min, respectively.

The oxidation experiments above the dissociation oxygen partial pressure of Wüstite were carried out with the Fe–1.9Mn–1.6Cr–0.1Si steel alloy in the same horizontal quartz tube, but with an infrared furnace (Model 4069-12R-05L, Research Inc.) at 950 °C for 8 h in a gas mixture of Ar + 20 vol% CO₂ + 20 vol% CO (oxygen partial pressure of 8.8×10^{-16} atm.; see “Appendix”) at atmospheric pressure with a total gas flow of 500 sccm. The temperature of the sample during annealing was determined by measuring the temperature of a dummy sample which was spot-welded to a thermocouple. The dummy sample has the same dimensions and chemical composition as the target sample.

Prior to admitting the gas mixtures to any of the furnaces, each gas, i.e. Ar, N₂, H₂, CO₂ and CO (all with a purity better than 5 N vol%), was filtered to remove any residual hydrocarbons, moisture and oxygen, with Accosorb (< 10 ppb hydrocarbons), Hydrosorb (< 10 ppb H₂O) and Oxysorb (< 5 ppb O₂) filters (Messer Griesheim, Germany), respectively. The flow of each gas was regulated and monitored using mass flow controllers (Bronkhorst, the Netherlands).

Characterization

Grazing angle X-ray diffractometry (GA-XRD) was used to identify the oxide phases present at the surface of the oxidized samples. The XRD patterns were recorded, with a Bruker D8 Discover diffractometer in the grazing incidence geometry using Co K α radiation, in the 2θ region between 20° and 60° with a step size of 0.03° 2θ and a dwell time of 10 s. The incidence angle of the X-ray beam was fixed at 3° with respect to the sample surface. In this grazing incidence geometry, the depth below the surface corresponding to 70% of the diffracted intensity of pure iron is 1.27–1.34 μm for 2θ ranging from 30° to 60° [12]. When the incidence angle of the X-ray beam was at 2° with respect to the sample surface, the depth below the surface corresponding to 70% of the diffracted intensity of FeO is 1.4–1.5 μm for 2θ ranging from 30° to 60°. Also, XRD measurements in the Bragg–Brentano geometry were taken with the same diffractometer in the 2θ region between 10° and 110° with a step size of 0.03° 2θ and a dwell time of 2 s. Then, the depth below the surface corresponding to 70% of the diffracted intensity of FeO for Bragg–Brentano geometry is about 5.7–10.9 μm for 2θ from 30° to 60° [12].

The surface and cross section of the annealed samples were observed with scanning electron microscopy (SEM) using a JSM-6500F (JEOL, Japan) operated with an accelerating voltage of 5 or 15 kV. X-ray microanalysis (XMA) using energy-dispersive spectroscopy (EDS) was performed with the same SEM instrument, but equipped with an UltraDry 30 mm² detector (Thermo Fisher Scientific, the USA) to determine the chemical composition of oxides qualitatively.

X-ray photoelectron spectroscopy (XPS) was used to analyse the chemical composition of the oxides at the steel surfaces. The photoelectron spectra were recorded with a PHI 5400 ESCA equipped with an X-ray source operated at 200 W and 13 kV using an Al anode. The pass energy of the spherical capacitor analyser was set at 35.75 eV. Prior to the recording of the spectra, the steel sample surface

was sputtered mildly with a 3 keV Ar ion beam with ion flux of 2×10^{-13} mol/mm² s, rastering over an area of 5×5 mm for 10 min.

Results and Discussion

Phase Diagrams and Oxide Phases

The phase diagrams of Fe–Mn, Fe–Mn–Cr and Fe–Mn–Cr–Si alloys in an oxidizing environment at 950 °C are shown in Figs. 1, 2, 3, 4, 5 and 6. These phase diagrams were constructed with FactSage [13]. The thermodynamic data of the stoichiometric compounds Cr₂O₃ and SiO₂ as well as the solid solution oxides, namely (Mn,Cr,Fe)₃O₄ spinel (Mn,Fe)O, (Mn,Fe)₂SiO₄ and (Mn,Fe)SiO₃, were taken from the FToxid database [14]. A solid solution of Fe–Mn binary, Fe–Mn–Cr ternary and Fe–Mn–Cr–Si quaternary alloy with fcc or bcc crystal lattice was created with the thermodynamic data in the FSstel database [14]. A gas mixture of Ar and O₂ with increasing oxygen partial pressure (in atm.) was created using the thermodynamic data in the FactPS database [15] to be in equilibrium with the alloy phase and the oxides.

First the oxide phase that can be formed in a Fe–Mn binary alloy is considered; see Fig. 1 and Table 2. The dissociation oxygen partial pressure of MnO is lower than that of FeO. However, since both FeO and MnO have the same rock-salt crystal structure, FeO and MnO can form a continuous solid solution [16] denoted as (Mn,Fe)O. The Fe concentration in the (Mn,Fe)O increases with oxygen partial pressure, which agrees with the results reported in Refs. [17, 18]. Above an oxygen partial pressure of about 1.6×10^{-16} atm. at 950 °C, all the Fe and Mn in the alloy are oxidized to (Mn,Fe)O. The prediction with the computed phase diagram is in agreement with our experimental results (see Table 2) and the results reported in Ref. [5], and (Mn,Fe)O is the only type of oxide phase that can be formed in a Fe–Mn binary alloy below an oxygen partial pressure of 1.6×10^{-16} atm. However, when annealing the Fe–1.7Mn steel at the dew point of -45 °C (oxygen partial

Fig. 1 Computed phase diagram of Fe–Mn binary alloys in an oxidizing environment at 950 °C. The squares indicate the Fe with 1.7 at.% Mn alloy oxidized at dew points of -45 and 10 °C, respectively

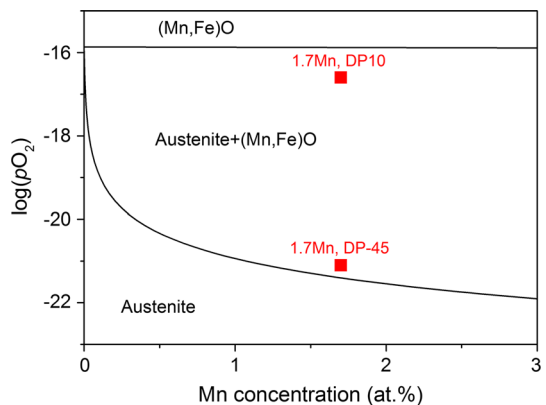


Fig. 2 Computed phase diagram of Fe–Mn–Cr alloys with Mn concentration fixed at 1.8 or 2.8 (dashed lines) at.% in an oxidizing environment at 950 °C. Note that dissociation oxygen partial pressure of (Mn,Fe)O slightly increases with Cr concentration in the alloy. The squares indicate the alloy with 0.6 or 1.1 at.% Cr oxidized at dew points of – 45 and 10 °C

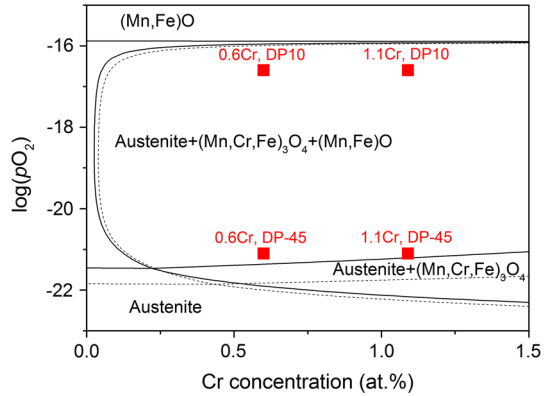


Fig. 3 Phase diagram of Fe–Mn–Cr–Si alloys with Si concentration fixed at 0.1 at.% and Mn concentration fixed at 1.8 at.% in an oxidizing environment at 950 °C. The squares indicate the alloy with 1.0 at.% Cr oxidized at dew points of – 45 and – 37 °C, respectively

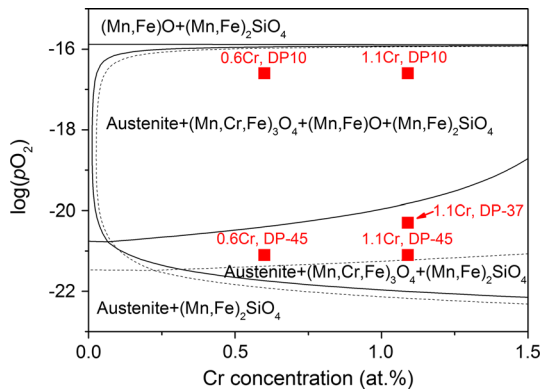
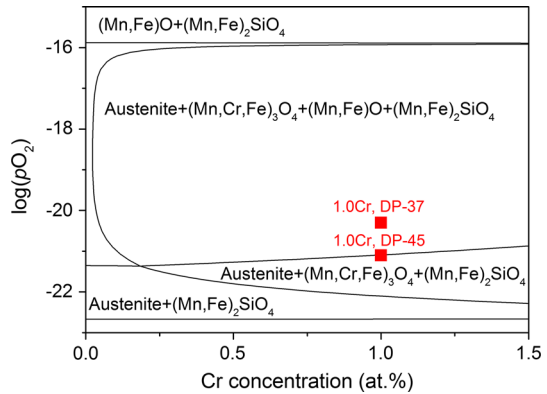


Fig. 4 Computed phase diagram of Fe–Mn–Cr–Si alloys with Si concentration fixed at 0.5 at.% and Mn concentration fixed at 1.8 or 2.8 (dashed lines) at.% in an oxidizing environment at 950 °C. The squares indicate the alloy with 0.6 or 1.1 at.% Cr oxidized at dew points of – 45, – 37 and 10 °C, respectively. (It is noted that when the Mn concentration in the steel alloy equals 1.8 at.% and the p_{O_2} is below 3.2×10^{-23} atm., the formation of $(Mn,Fe)SiO_3$ is also predicted, but is not shown here.)

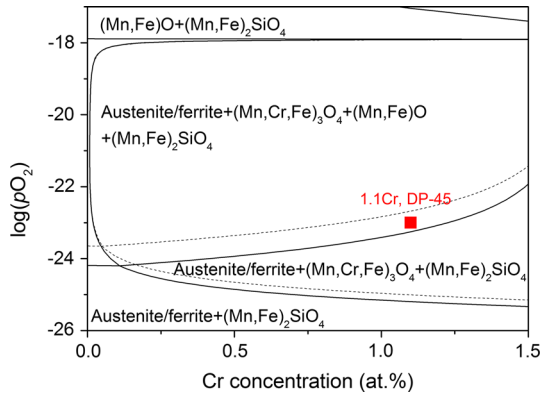
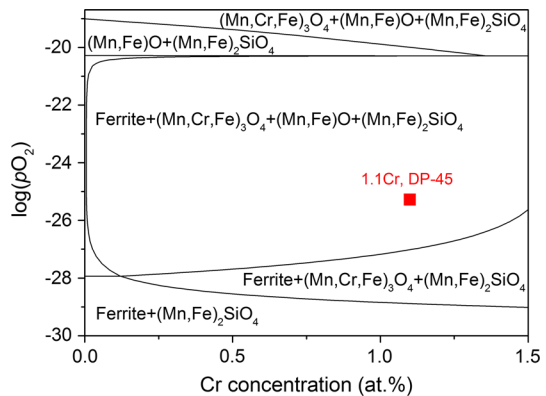


Fig. 5 Computed phase diagram of Fe–Mn–Cr–Si alloys with bcc (ferrite) or fcc (austenite, dashed lines) crystal lattice with Mn and Si concentrations fixed at 1.8 and 0.5 at.%, respectively, in an oxidizing environment at 850 °C. The square indicates the alloy with 1.1 at.% Cr oxidized at the dew point of –45 °C. (It is noted that when the alloy matrix is in austenite and the p_{O_2} is below 3.2×10^{-26} atm., the formation of $(\text{Mn,Fe})\text{SiO}_3$ is also predicted, but is not shown here.)

Fig. 6 Computed phase diagram of Fe–Mn–Cr–Si alloys with bcc (ferrite) crystal lattice with Mn and Si concentrations fixed at 1.8 and 0.5 at.%, respectively, in an oxidizing environment at 750 °C. The square indicates the alloy with 1.1 at.% Cr oxidized at the dew point of –45 °C



pressure of 8.1×10^{-22} atm.), the $(\text{Mn,Fe})\text{O}$ cannot be identified with GA-XRD because the amount of oxides formed is too small.

The oxide species formed in Fe–Mn–Cr ternary alloys at 950 °C as a function of oxygen partial pressure and Cr concentration in the range of 0–1.5 at.% for a fixed Mn concentration of 1.8 at.% were predicted; see Fig. 2. Adding Cr to the Fe–Mn alloy leads to the formation of MnCr_2O_4 spinel with a cubic crystal lattice. However, Fe cations can substitute with Mn and Cr cations in the spinel to form an oxide solution denoted as $(\text{Mn,Cr,Fe})_3\text{O}_4$. For the alloy compositions considered here, changing the Cr concentration and oxygen partial pressure does not result in the formation of Cr_2O_3 , which is in agreement with our experimental results; see Table 2. Considering the Mn concentration in the alloy fixed, the dissociation oxygen partial pressure of $(\text{Mn,Cr,Fe})_3\text{O}_4$ spinel decreases, while the dissociation oxygen partial pressure of $(\text{Mn,Fe})\text{O}$ slightly increases with the Cr concentration in the alloy; see Fig. 2. The dissociation partial pressure of $(\text{Mn,Cr,Fe})_3\text{O}_4$ spinel is

Table 2 Identified oxide species from XRD measurements (all XRD results obtained from measurements using Co K α radiation with grazing incidence geometry) after annealing the Fe–Mn and Fe–Mn–Cr–(Si) steel alloys at 950 °C for 1 h in a gas mixture of Ar or N $_2$ with 5 vol% H $_2$ and dew points of – 45, – 37, – 30, – 10 and 10 °C (corresponding to oxygen partial pressures (p_{O_2}) of 8.1×10^{-22} , 5.0×10^{-21} , 2.2×10^{-20} , 1.0×10^{-18} and 2.3×10^{-17} atm., respectively)

Sample	P_{O_2} 8.1×10^{-22} (atm.)	P_{O_2} 5.0×10^{-21} (atm.)	P_{O_2} 2.2×10^{-20} (atm.)	P_{O_2} 1.0×10^{-18} (atm.)	P_{O_2} 2.3×10^{-17} (atm.)
Fe–1.7Mn	NA ^a	(Mn,Fe)O	(Mn,Fe)O	(Mn,Fe)O	(Mn,Fe)O
Fe–1.8Mn– 0.5Cr	(Mn,Cr,Fe) $_3$ O $_4$	(Mn,Cr,Fe)$_3$O$_4^*$	(Mn,Cr,Fe)$_3$O$_4^*$	(Mn,Cr,Fe)$_3$O$_4^*$	(Mn,Cr,Fe)$_3$O$_4^*$
	(Mn,Fe)O	(Mn,Fe)O*	(Mn,Fe)O*	(Mn,Fe)O*	(Mn,Fe)O*
Fe–1.7Mn– 1.5Cr	(Mn,Cr,Fe) $_3$ O $_4$	(Mn,Cr,Fe) $_3$ O $_4$	(Mn,Cr,Fe)$_3$O$_4^*$	(Mn,Cr,Fe)$_3$O$_4^*$	(Mn,Cr,Fe)$_3$O$_4^*$
		(Mn,Fe)O	(Mn,Fe)O*	(Mn,Fe)O*	(Mn,Fe)O*
Fe–1.8Mn– 0.6Cr– 0.5Si	(Mn,Fe) $_2$ SiO $_4$	(Mn,Cr,Fe) $_3$ O $_4$	(Mn,Cr,Fe) $_3$ O $_4$	(Mn,Cr,Fe) $_3$ O $_4$	(Mn,Cr,Fe) $_3$ O $_4$
		(Mn,Fe) $_2$ SiO $_4$	(Mn,Fe)O	(Mn,Fe)O	(Mn,Fe)O
			(Mn,Fe) $_2$ SiO $_4$	(Mn,Fe) $_2$ SiO $_4$	(Mn,Fe) $_2$ SiO $_4$
Fe–1.8Mn– 1.1Cr– 0.5Si	(Mn,Fe) $_2$ SiO $_4$	(Mn,Cr,Fe) $_3$ O $_4$	(Mn,Cr,Fe) $_3$ O $_4$	(Mn,Cr,Fe) $_3$ O $_4$	(Mn,Cr,Fe) $_3$ O $_4$
		(Mn,Fe) $_2$ SiO $_4$	(Mn,Fe) $_2$ SiO $_4$	(Mn,Fe)O	(Mn,Fe)O
			(Mn,Fe) $_2$ SiO $_4$	(Mn,Fe) $_2$ SiO $_4$	(Mn,Fe) $_2$ SiO $_4$
Fe–1.9Mn– 1.0Cr– 0.1Si	(Mn,Cr,Fe) $_3$ O $_4$	(Mn,Cr,Fe) $_3$ O $_4$	(Mn,Cr,Fe)$_3$O$_4^*$	(Mn,Cr,Fe)$_3$O$_4^*$	(Mn,Cr,Fe)$_3$O$_4^*$
		(Mn,Fe)O	(Mn,Fe)O*	(Mn,Fe)O*	(Mn,Fe)O*
Fe–1.9Mn– 1.6Cr– 0.1Si	(Mn,Cr,Fe) $_3$ O $_4$	(Mn,Cr,Fe) $_3$ O $_4$	(Mn,Cr,Fe)$_3$O$_4^*$	(Mn,Cr,Fe)$_3$O$_4^*$	(Mn,Cr,Fe)$_3$O$_4^*$
		(Mn,Fe)O	(Mn,Fe)O*	(Mn,Fe)O*	(Mn,Fe)O*
Fe–2.8Mn– 0.6Cr– 0.5Si	(Mn,Cr,Fe) $_3$ O $_4$	(Mn,Cr,Fe)$_3$O$_4^*$	(Mn,Cr,Fe) $_3$ O $_4$	(Mn,Cr,Fe) $_3$ O $_4$	(Mn,Cr,Fe) $_3$ O $_4$
	(Mn,Fe)O	(Mn,Fe)O*	(Mn,Fe)O	(Mn,Fe)O	(Mn,Fe)O
	(Mn,Fe) $_2$ SiO $_4$	(Mn,Fe)$_2$SiO$_4^*$	(Mn,Fe) $_2$ SiO $_4$	(Mn,Fe) $_2$ SiO $_4$	(Mn,Fe) $_2$ SiO $_4$

Predicted oxide phases are denoted in bold and indicated with an asterisk

^aData not available because the amount of oxides formed is below the detection limit of the XRD measurements

* Predicted oxide phases

lower than the dissociation oxygen partial pressure of (Mn,Fe)O, when the Cr concentration in the bulk alloy is higher than about 0.2 at.%. This is confirmed by the observation that (Mn,Cr,Fe) $_3$ O $_4$ spinel is formed during annealing at low dew points, while (Mn,Fe)O appears at high dew points in the Fe–1.7Mn–1.5Cr, Fe–

1.9Mn–1.0Cr–0.1Si and Fe–1.9Mn–1.6Cr–0.1Si steel alloys; see Table 2. The increase in the dissociation oxygen partial pressure of (Mn,Fe)O with the Cr concentration is evidenced by the identification of (Mn,Fe)O in the Fe–1.8Mn–0.5Cr, but is not detected in the Fe–1.7Mn–1.5Cr alloy annealed at the dew point of $-45\text{ }^{\circ}\text{C}$; see Table 2. This is due to the fact that the dissociation oxygen partial pressure of (Mn,Fe)O decreases with the concentration of Mn dissolved in the alloy. At certain oxygen partial pressure and concentration of Mn in the alloy, the amount of Mn that reacts with Cr to form (Mn,Cr,Fe)₃O₄ spinel increases and, hence, the concentration of Mn that remains in the alloy decreases with Cr concentration.

The addition of Si to the Fe–Mn–Cr alloys leads to the formation of (Mn,Fe)₂SiO₄. The dissociation oxygen partial pressure of (Mn,Fe)₂SiO₄ is lower than that of (Mn,Cr,Fe)₃O₄ for the alloy compositions considered here; see Figs. 3 and 4. This is consistent with the oxide phase identified in the annealed Fe–1.8Mn–0.6Cr–0.5Si and Fe–1.8Mn–1.1Cr–0.5Si steels, i.e. a single (Mn,Fe)₂SiO₄ oxide phase is formed at the dew point of $-45\text{ }^{\circ}\text{C}$; see Table 2. However, according to the phase diagram (Fig. 4), the formation of (Mn,Cr,Fe)₃O₄ spinel is also predicted for the Fe–1.8Mn–0.6Cr–0.5Si and Fe–1.8Mn–1.1Cr–0.5Si alloys after annealing at the dew point of $-45\text{ }^{\circ}\text{C}$. This shows that adding Si to the Fe–Mn–Cr steel alloys suppresses the formation of (Mn,Cr,Fe)₃O₄ spinel. Apparently, Si in the steel lowers the oxygen partial pressure at steel surface. But, after annealing of the Fe–1.8Mn–0.6Cr–0.5Si and Fe–1.8Mn–1.1Cr–0.5Si alloys at higher dew points than $-45\text{ }^{\circ}\text{C}$ up to $10\text{ }^{\circ}\text{C}$, also (Mn,Cr,Fe)₃O₄ spinel is observed; see Table 2. This is in agreement with the phase diagram; see Fig. 4.

With 1.8 at.% Mn and 0–1.5 at.% Cr in the bulk alloy, the dissociation oxygen partial pressure of (Mn,Fe)O in the Fe–Mn–Cr–Si ternary alloys increases with Si concentration; see Figs. 3 and 4. For example, for a fixed Mn and Cr concentration of 1.8 and 1.0 at.%, respectively, the dissociation oxygen partial pressure of (Mn,Fe)O increases from about 8.1×10^{-22} to 1.0×10^{-20} atm. with increasing Si concentration from 0.1 to 0.5 at.% at $950\text{ }^{\circ}\text{C}$. This corresponds to the experimental observation that (Mn,Fe)O is formed in the Fe–1.8Mn–1.0Cr–0.5Si at a higher annealing dew point than in the Fe–1.9Mn–1.0Cr–0.1Si steel alloy; see Table 2. The effect of Si on the dissociation oxygen partial pressure of (Mn,Fe)O can be explained as follows. Since (Mn,Fe)₂SiO₄ is much more stable than both (Mn,Cr,Fe)₃O₄ spinel and (Mn,Fe)O, the concentration of Si in the alloy matrix is practically zero at the dissociation oxygen partial pressure of (Mn,Cr,Fe)₃O₄ spinel and (Mn,Fe)O. Thus, the concentration of Mn that remains in the alloy matrix decreases with the amount of Si added to the alloy due to the formation of (Mn,Fe)₂SiO₄. Hence, the dissociation oxygen partial pressure of (Mn,Fe)O increases.

Adding Mn in the Fe–Mn–Cr–(Si) alloy decreases the dissociation oxygen partial pressure of (Mn,Fe)O and (Mn,Cr,Fe)₃O₄ spinel; see Figs. 2 and 4. Both (Mn,Cr,Fe)₃O₄ spinel and (Mn,Fe)O are formed in the Fe–2.8Mn–0.5Cr–0.5Si steel after annealing at $950\text{ }^{\circ}\text{C}$ in the gas mixture with the dew point of $-45\text{ }^{\circ}\text{C}$, while only (Mn,Fe)₂SiO₄ is formed in the Fe–1.8Mn–0.5Cr–0.5Si steel after annealing under the same condition. This clearly shows that increasing Mn

concentration in the steel alloy promotes the formation of $(\text{Mn,Cr,Fe})_3\text{O}_4$ spinel and $(\text{Mn,Fe})\text{O}$.

Between the dissociation oxygen partial pressure of $(\text{Mn,Fe})\text{O}$ and 2.3×10^{-17} atm. (dew point of 10°C) at 950°C , the effect of oxygen partial pressure has no effect on the type of oxides formed during annealing of Fe–Mn–Cr–(Si) steel alloys. For example, both $(\text{Mn,Fe})\text{O}$ and $(\text{Mn,Cr,Fe})_3\text{O}_4$ spinel were identified on Fe–1.8Mn–0.6Cr–0.5Si, Fe–1.8Mn–1.1Cr–0.5Si and Fe–2.8Mn–0.6Cr–0.5Si steels after annealing at -10 and 10°C ; see Table 2. It is expected that annealing the Fe–1.8Mn–0.5Cr, Fe–1.7Mn–1.5Cr, Fe–1.9Mn–1.0Cr–0.1Si, Fe–1.9Mn–1.6Cr–0.1Si and Fe–2.8Mn–0.6Cr–0.5Si steel alloys above the dissociation oxygen partial pressure of $(\text{Mn,Fe})\text{O}$ results in the formation of both $(\text{Mn,Fe})\text{O}$ and $(\text{Mn,Cr,Fe})_3\text{O}_4$ spinel; cf. Figs. 2 and 3.

The effect of the crystal lattice of the steel matrix on the equilibrium oxide phases formed in advanced high-strength steels is small. Figure 5 shows the computed phase diagrams of the Fe–Mn–Cr–Si quaternary alloys in an oxidizing gas atmosphere at 850°C with the concentration of Mn and Si fixed at 1.8 and 0.5 at.%, respectively. The constitution of the steel alloy matrix was fixed in either bcc or fcc phase in the computation, and thus the effect of alloy composition on the austenite–ferrite phase transformation was not considered. The dissociation oxygen partial pressure of $(\text{Mn,Cr,Fe})_3\text{O}_4$ spinel and $(\text{Mn,Fe})\text{O}$ at 850°C in austenite is only slightly higher than in ferrite. This is due to the fact that the chemical potential of the alloying elements Mn and Cr in ferrite is higher than that in austenite. For example, according to the computation results for the Fe–1.8 at.% Mn–1.5 at.% Cr alloy at 850°C , the chemical potential of Mn and Cr in ferrite is -92.0 and -73.5 kJ/mol, respectively, while the chemical potential of Mn and Cr in austenite is -97.3 and -74.5 kJ/mol, respectively. For the same crystal lattice of the steel matrix, the dissociation oxygen partial pressure of both $(\text{Mn,Cr,Fe})_3\text{O}_4$ spinel and $(\text{Mn,Fe})\text{O}$ increases with temperature; see Figs. 5 and 6. The oxides identified in the Fe–1.8Mn–1.0Cr–0.5Si steel alloy after annealing at 750°C in a gas mixture with the dew point of -45°C are as follows: $(\text{Mn,Fe})_2\text{SiO}_4$, $(\text{Mn,Cr,Fe})_3\text{O}_4$ spinel and $(\text{Mn,Fe})\text{O}$. However, the oxides identified in the same steel annealed at 850°C at the same dew point are $(\text{Mn,Fe})_2\text{SiO}_4$ and $(\text{Mn,Cr,Fe})_3\text{O}_4$ spinel. The type of identified oxide phases is in agreement with the predictions from the computed phase diagrams; see Figs. 5 and 6.

Composition of Oxide Phases

The Fe concentration in the $(\text{Mn,Cr,Fe})_3\text{O}_4$ spinel formed during the oxidation of Fe–Mn–Cr steel alloys increases with ambient oxygen partial pressure. A spinel oxide can be written in the general form of AB_2O_4 [19]. For MnCr_2O_4 spinel, Fe cations can substitute both Mn cations at A-site and Cr cations at B-site [20]. The lattice constant of $(\text{Mn}_{1-x}\text{Fe}_x)(\text{Cr}_{2-y}\text{Fe}_y)\text{O}_4$ spinel increases with the value of y , but decreases with the value of x [20]. The amount of Fe dissolved in the $(\text{Mn,Cr,Fe})_3\text{O}_4$ spinel (i.e. the value of $(x+y)/3$ in $(\text{Mn}_{1-x}\text{Fe}_x)(\text{Cr}_{2-y}\text{Fe}_y)\text{O}_4$) can be predicted [13, 15]. For example, the amount of Fe in $(\text{Mn,Cr,Fe})_3\text{O}_4$ increases from 0 to 0.12 when annealing a Fe–1.8 at.% Mn–1.1 at.% Cr alloy at 950°C in Ar + 5 vol% H_2

gas mixture while increasing the dew point from -45 to 10 °C; see Fig. 7. Moreover, the calculations show that non-stoichiometry of the spinel is negligible and that the Fe dissolved in the $(\text{Mn}_{1-x}\text{Fe}_x)(\text{Cr}_{2-y}\text{Fe}_y)\text{O}_4$ spinel mainly resides at the A-site after annealing at 950 °C with an oxygen partial pressure of 2.3×10^{-17} atm. (i.e. corresponding to a dew point of 10 °C in Ar + 5 vol% H_2 gas mixture). The measured stress-free lattice constant of $(\text{Mn,Cr,Fe})_3\text{O}_4$ spinel formed in the Fe–1.9Mn–1.6Cr–0.1Si steel is 843.1 ± 0.2 and 841.3 ± 0.1 pm after annealing at 950 °C for 16 h in a gas mixture of Ar + 5 vol% H_2 with dew points of -45 and 10 °C, respectively. This decrease in the lattice constant of the $(\text{Mn,Cr,Fe})_3\text{O}_4$ spinel with increasing annealing dew point is attributed to an increasing amount of Fe dissolved into the $(\text{Mn,Cr,Fe})_3\text{O}_4$ spinel [20]. It is also predicted that the concentration of Fe in $(\text{Mn,Fe})\text{O}$ formed during oxidation of Fe–Mn–Cr steel alloys increases with the dew point of the annealing ambient; see Fig. 7.

The $(\text{Mn,Cr,Fe})_3\text{O}_4$ spinel transforms into $(\text{Mn,Fe})_{1-x}\text{Cr}_x\text{O}$ at high oxygen partial pressures, close to the dissociation oxygen partial pressure of Wüstite; see Figs. 2, 3, 4, 5 and 6. For example, the $(\text{Mn,Cr,Fe})_3\text{O}_4$ spinel starts to transform into $(\text{Mn,Fe})_{1-x}\text{Cr}_x\text{O}$ above an oxygen partial pressure of about 6.3×10^{-17} atm. (dew point of 18 °C) at 950 °C for the Fe–1.8 at.% Mn–1.1 at.% Cr alloy; see Fig. 8. This is because $(\text{Mn,Fe})\text{O}$ can dissolve small amount of Cr (x below about 0.03 in $(\text{Mn,Fe})_{1-x}\text{Cr}_x\text{O}$ at 950 °C). The value of x in $(\text{Mn,Fe})_{1-x}\text{Cr}_x\text{O}$ increases from about 0.013 to 0.027 with increasing oxygen partial pressure from 10^{-20} to 10^{-16} atm. at 950 °C; see Fig. 7. At relatively low oxygen partial pressure (say below 10^{-17} atm.) the amount of $(\text{Mn,Fe})\text{O}$ formed in the alloy is small and the oxidized Cr is mainly present as $(\text{Mn,Cr,Fe})_3\text{O}_4$ spinel. However, with increasing oxygen partial pressure the amount of $(\text{Mn,Fe})\text{O}$ increases due to the increasing amount of Fe in the matrix being oxidized; see Figs. 7 and 8. Hence, the amount of Cr dissolved in $(\text{Mn,Fe})\text{O}$ increases, while the amount of Cr in $(\text{Mn,Cr,Fe})_3\text{O}_4$ spinel decreases. Above oxygen

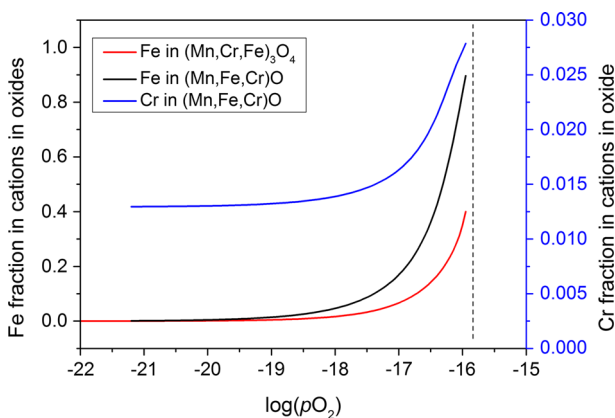
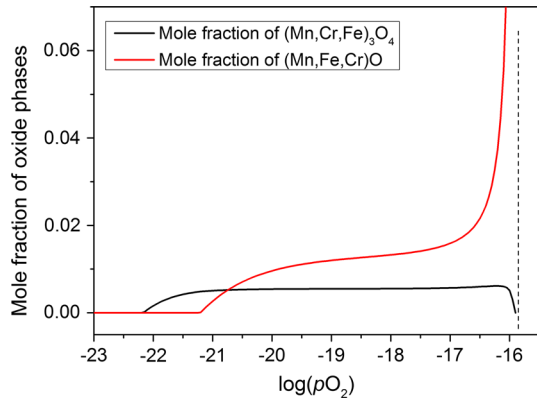


Fig. 7 Computed composition of $(\text{Mn,Cr,Fe})_3\text{O}_4$ spinel and $(\text{Mn,Fe,Cr})\text{O}$ monoxide as a function of oxygen partial pressure (in atm.) formed in the Fe–1.8 at.% Mn–1.1 at.% Cr alloy at 950 °C. Dashed line indicates the dissociation oxygen partial pressure of FeO (Wüstite)

Fig. 8 Computed mole fraction of $(\text{Mn,Cr,Fe})_3\text{O}_4$ spinel and $(\text{Mn,Fe,Cr})\text{O}$ monoxide as a function of oxygen partial pressure (in atm.) in the Fe–1.8 at.% Mn–1.1 at.% Cr alloy at 950 °C. Dashed line indicates the dissociation oxygen partial pressure of Wüstite



partial pressure of about 1.3×10^{-16} atm. (dew point of 23 °C), $(\text{Mn,Fe})_{1-x}\text{Cr}_x\text{O}$ is the only type of oxide formed.

An oxide scale is formed at the surface of the Fe–1.9Mn–1.6Cr–0.1Si steel after annealing at 950 °C for 8 h in the Ar + 20 vol% CO_2 + 20 vol% CO gas mixture, i.e. at an oxygen partial pressure of 8.8×10^{-16} atm. This oxide scale fully covers the steel surface, but the scale thickness is not uniform; see Fig. 9. An internal oxidation zone is formed underneath the oxide scale. $(\text{Mn,Cr,Fe})_3\text{O}_4$ spinel, MnO and Wüstite were identified from the diffraction pattern obtained by XRD with Bragg–Brentano geometry. However, in the diffraction pattern recorded by XRD using the grazing incidence geometry (having a smaller analysis depth), $(\text{Mn,Cr,Fe})_3\text{O}_4$ spinel and MnO can hardly be observed and the relative intensity of the diffraction peak of iron is significantly lower; see Fig. 10. This shows that the diffraction pattern recorded by XRD using the grazing incidence geometry mainly contains the information of the oxide scale at steel surface. These observations suggest that the external oxide scale is composed of Wüstite only, while the $(\text{Mn,Cr,Fe})_3\text{O}_4$ spinel and $(\text{Mn,Fe})\text{O}$ are formed as internal oxide precipitates.

Fig. 9 SEM backscattered electron image of cross section of the Fe–1.9Mn–1.6Cr–0.1Si steel annealed at 950 °C for 8 h in a gas mixture of Ar + 20 vol% CO_2 + 20 vol% CO (oxygen partial pressure of 8.8×10^{-16} atm.). A Wüstite scale fully covers the steel surface after oxidation. An internal oxidation zone (IOZ) is formed beneath the Wüstite scale

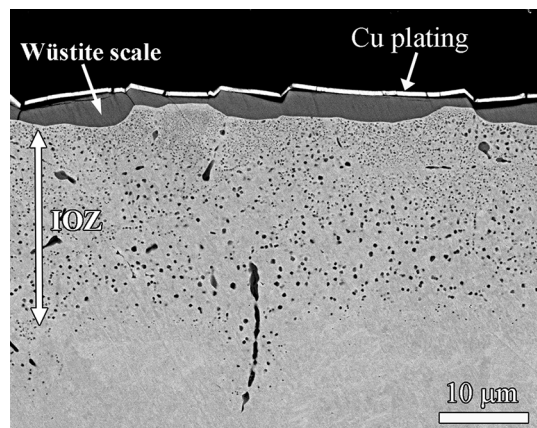
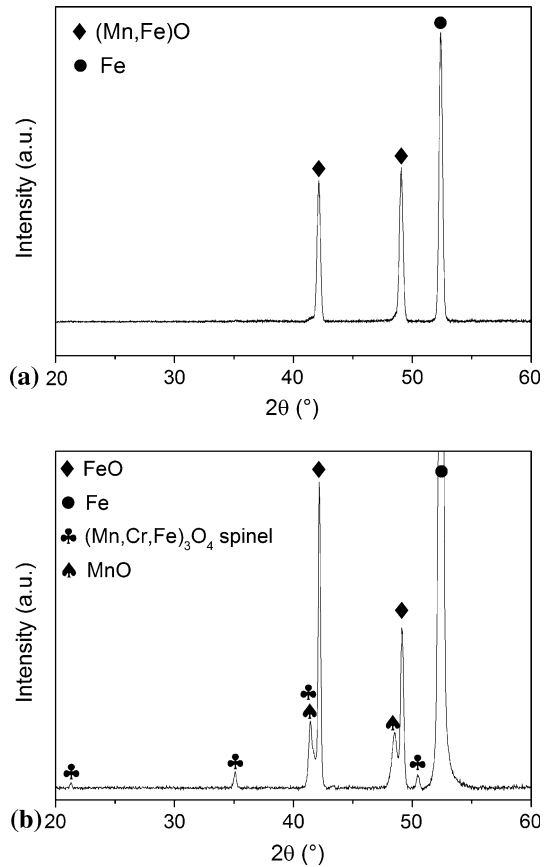


Fig. 10 XRD patterns of the Fe–1.9Mn–1.6Cr–0.1Si steel annealed at 950 °C for 8 h in a gas mixture of Ar + 20 vol% CO₂ + 20 vol% CO (oxygen partial pressure of 8.8×10^{-16} atm.; cf. Fig. 9); measured with **a** grazing incidence geometry and **b** Bragg–Brentano geometry



Moreover, the Cr $2p$ and Mn $2p$ lines observed with XPS suggest that both Cr and Mn are dissolved in the Wüstite. Thus, the scale is composed of $(\text{Mn,Fe})_{1-x}\text{Cr}_x\text{O}$ oxide solid solution. According to the XPS analysis the value of x in the $(\text{Mn,Fe})_{1-x}\text{Cr}_x\text{O}$ scale is about 0.02, which is in reasonable agreement with thermodynamic prediction; see Fig. 7.

The establishment of local thermodynamic equilibrium between oxide precipitates and dissolved oxygen in alloy matrix upon internal oxidation of Fe–Mn binary steel alloys has been reported [18]. For Fe–Mn–Cr–(Si) steel alloys, the agreement between the computed phase diagrams and the experimentally identified oxide species formed during annealing at different temperatures and oxygen partial pressure indicates that (local) thermodynamic equilibrium between the gas ambient and the steel surface was established. Finally, the thermodynamic data used allowed the prediction of the oxide formed in advanced high-strength steels having a complex composition and microstructure.

Fig. 11 SEM backscattered electron images of cross section of the Fe-1.9Mn-1.6Cr-0.1Si steel annealed for 1 h at 950 °C in a gas mixture of Ar or N₂ with 5 vol% H₂ and dew points of **a** - 45 °C and **b** 10 °C (oxygen partial pressure of 8.1×10^{-22} and 2.3×10^{-17} atm., respectively). At the dew point of - 45 °C (Mn,Cr,Fe)₃O₄ is formed, and at the dew point of 10 °C both (Mn,Cr,Fe)₃O₄ and (Mn,Fe)O are formed

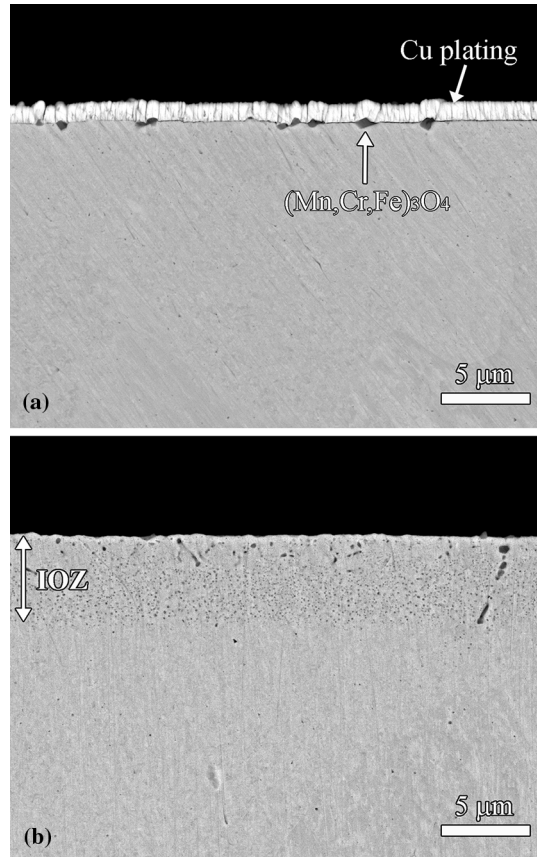
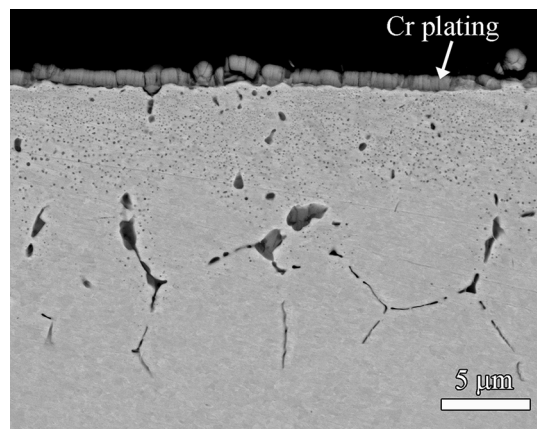


Fig. 12 SEM backscattered electron image of cross section of the Fe-1.8Mn-1.1Cr-0.5Si steel annealed for 1 h at 950 °C in a gas mixture of N₂ + 5 vol% H₂ at the dew point of 10 °C (oxygen partial pressure of 2.3×10^{-17} atm.). (Mn,Cr,Fe)₃O₄ and (Mn,Fe)O are formed, and (Mn,Fe)₂SiO₄ along the grain boundaries



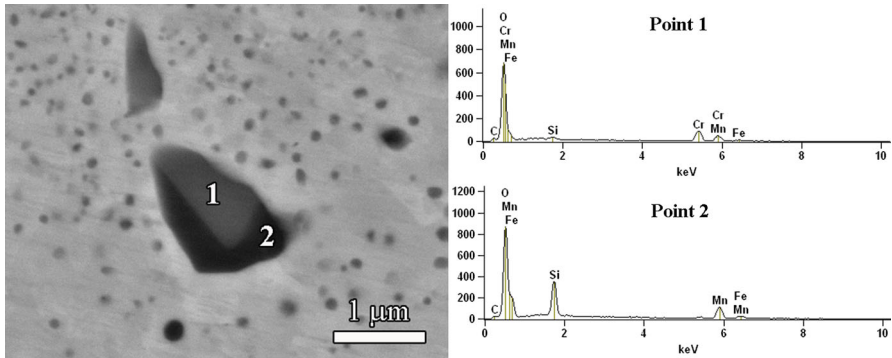


Fig. 13 Backscattered electron image of cross section of the Fe–1.8Mn–1.1Cr–0.5Si steel annealed for 1 h at 950 °C in a gas mixture of N₂ + 5 vol% H₂ at the dew point of 10 °C (oxygen partial pressure of 2.3×10^{-17} atm.), and spectrums of characteristic X-rays measured with XMA on two different locations on an oxide precipitate. Oxide precipitates in Fe–Mn–Cr–Si quaternary steel alloys may consist of both (Mn,Cr,Fe)₃O₄ spinel and (Mn,Fe)₂SiO₄

Fig. 14 SEM backscattered electron images of surface of **a** Fe–1.7Mn and **b** Fe–1.9Mn–1.6Cr–0.1Si steel annealed for 1 h at 950 °C in a mixture of Ar + 5 vol% H₂ gases at the dew point of –45 °C (oxygen partial pressure of 8.1×10^{-22} atm.). Cr promotes formation of (Mn,Cr,Fe)₃O₄ along the grain boundaries at the surface

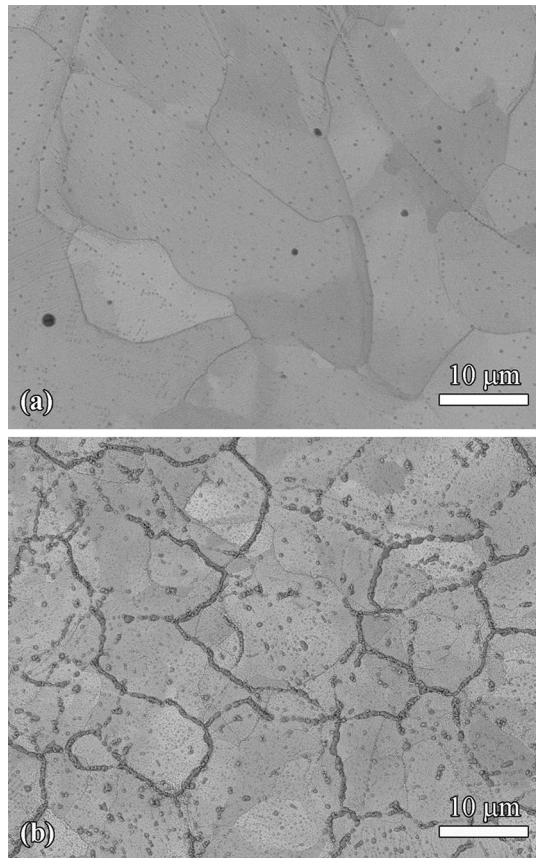
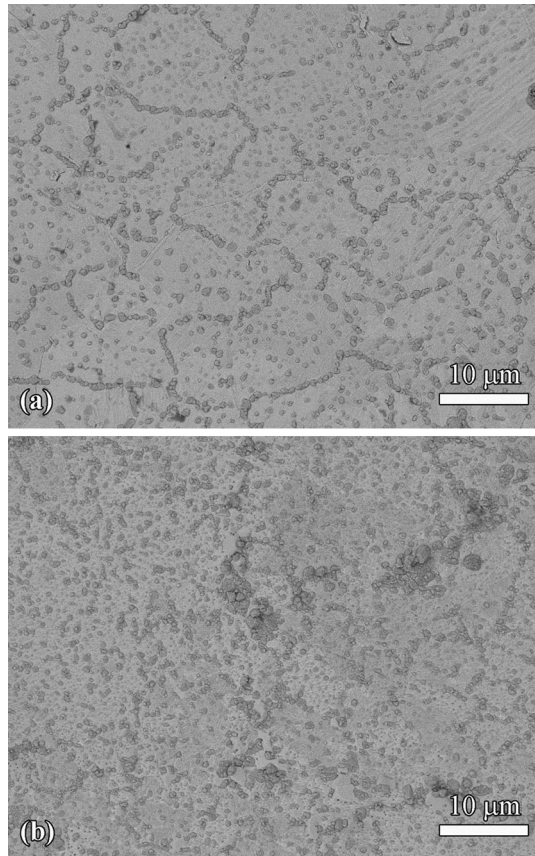


Fig. 15 SEM backscattered electron images of surface of **a** Fe–1.7Mn and **b** Fe–1.9Mn–1.6Cr–0.1Si steels annealed for 1 h at 950 °C in a gas mixture of Ar + 5 vol% H₂ at the dew point of 10 °C (oxygen partial pressure of 2.3×10^{-17} atm.)



Internal and External Oxides

The oxidation mode of Fe–Mn–Cr steel alloys annealed at 950 °C in a gas mixture of Ar or N₂ + 5 vol% H₂ changes from external to internal oxidation with increasing dew point from – 45 to 10 °C, which is similar as for Fe–Mn steels [5]. For example, when annealing the Fe–1.9Mn–1.6Cr–0.1Si steel in an Ar + 5 vol% H₂ gas mixture with the dew point of – 45 °C the oxides are formed mainly at the sample surface; see Fig. 11. Increasing the dew point of the annealing gas mixture to 10 °C, an internal oxidation zone is observed below the Fe–1.9Mn–1.6Cr–0.1Si steel surface. According to XMA and thermodynamic computations, the internal oxide precipitates should be composed of (Mn,Fe)O and (Mn,Cr,Fe)₃O₄ spinel. Adding Si to the Fe–Mn–Cr steel promotes the formation of (Mn,Fe)₂SiO₄ along original austenite grain boundaries; see Fig. 12. However, (Mn,Fe)₂SiO₄ also forms inside grains and an individual precipitate can be composed of more than one type of oxide species; see Fig. 13.

Adding Cr to a Fe–Mn binary steel alloy increases the amount of oxides formed at the steel surface; see, for example, Fig. 14. Oxides at the surface of the Fe–

1.9Mn–1.6Cr–0.1Si steel are formed both along grain boundaries and inside grains during annealing; see Fig. 14. According to the results of XMA, XRD and thermodynamic computations, the oxides at the surface of the Fe–1.9Mn–1.6Cr–0.1Si steel (along grain boundaries and inside grains) annealed at the dew point – 45 °C are composed of (Mn,Cr,Fe)₃O₄ spinel. A small amount of (Mn,Fe)₂SiO₄ is also formed along grain boundaries at the surface of the Fe–1.9Mn–1.6Cr–0.1Si steel as confirmed with XMA. The tendency of oxides formation along grain boundaries at the Fe–1.9Mn–1.6Cr–0.1Si steel surface decreases with dew point; see Figs. 14 and 15.

Conclusion

The oxide species formed during annealing of advanced high-strength steel can be well predicted by thermodynamic computation, since (local) thermodynamic equilibrium is established between the annealing gas ambient and the steel surface. Adding Cr to the Fe–Mn-based steel alloys results in the formation of (Mn,Cr,Fe)₃O₄ spinel during annealing. The dissociation oxygen partial pressure of (Mn,Cr,Fe)₃O₄ spinel is lower than that of (Mn,Fe)O. Increasing the Mn concentration in the alloy promotes the formation of (Mn,Cr,Fe)₃O₄ spinel and (Mn,Fe)O, which is associated with a decreasing dissociation oxygen partial pressures. The Si in the Fe–Mn–Cr steel alloys leads to the formation of (Mn,Fe)₂SiO₄ both along grain boundaries and inside grains during annealing. Increasing the Si concentration in the Fe–Mn–Cr steel alloy suppresses the formation of (Mn,Cr,Fe)₃O₄ spinel and (Mn,Fe)O. However, the formation of (Mn,Fe)₂SiO₄ can be mitigated by increasing the Mn concentration in the steel alloy. The amount of Fe dissolved in (Mn,Cr,Fe)₃O₄ spinel formed in Fe–Mn–Cr steels increases with annealing dew point. (Mn,Fe)O can dissolve only a small amount of Cr. Adding Cr to the Fe–Mn steel has no effect on the transition from external to internal oxidation, but increases the amount of oxides formed at steel surface during annealing.

Acknowledgements This research was carried out under the Project No. M22.3.11439 in the framework of the Research Program of the Materials innovation institute (M2i). Financial support from International Zinc Association (IZA) for the program ZCO-62 is gratefully acknowledged. The authors are indebted to Dr. W. Melfo of Tata Steel (Ijmuiden, the Netherlands) for providing the Mn-alloyed steels and the composition analysis. The authors are also indebted to Ing. J.C. Brouwer and Dr. ir. V.A. Lashgari for technical support and assistance with experiments.

Open Access This article is distributed under the terms of the Creative Commons Attribution 4.0 International License (<http://creativecommons.org/licenses/by/4.0/>), which permits unrestricted use, distribution, and reproduction in any medium, provided you give appropriate credit to the original author(s) and the source, provide a link to the Creative Commons license, and indicate if changes were made.

Appendix

The relation between dew point (DP) and partial pressure of water vapour ($p_{\text{H}_2\text{O}}$) was adopted from Ref. [21]:

$$\log p_{\text{H}_2\text{O}} = \frac{9.8\text{DP}}{273.8 + \text{DP}} - 2.22 \quad \text{DP} \leq 0 \text{ } ^\circ\text{C}$$

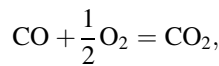
$$\log p_{\text{H}_2\text{O}} = \frac{7.58\text{DP}}{240 + \text{DP}} - 2.22 \quad \text{DP} > 0 \text{ } ^\circ\text{C},$$

where the units of $p_{\text{H}_2\text{O}}$ and DP are in atmosphere (atm.) and degree Celsius ($^\circ\text{C}$), respectively. Then, the partial pressure of oxygen (p_{O_2}) at equilibrium can be calculated with the Gibbs free energy of formation of water vapour, namely [21]:

$$\log p_{\text{O}_2} = 6 - \frac{26176}{T} + 2 \log \left(\frac{p_{\text{H}_2\text{O}}}{p_{\text{H}_2}} \right),$$

in which T is absolute temperature in Kelvin and p_{H_2} is the partial pressure of H_2 in atmosphere.

The p_{O_2} in a $\text{CO}_2 + \text{CO}$ gas mixture can be calculated considering the following reaction:



with the standard Gibbs free energy (unit in J/mol) expressed as:

$$\Delta G^0 = -282420 + 86.8T.$$

At equilibrium, the relation between CO_2/CO ratio and the p_{O_2} in the gas mixture can be calculated according to:

$$p_{\text{O}_2} = \left(\frac{p_{\text{CO}_2}}{p_{\text{CO}}} \right)^2 \exp \left(\frac{2\Delta G^0}{RT} \right).$$

References

1. N. Fonstein, *Advanced High Strength Sheet Steels*, (Springer, Zurich, 2015).
2. A. R. Marder, *Progress in Materials Science* **45**, 2000 (191).
3. G. M. Song, T. Vystavel, N. van der Pers, J. T. M. De Hosson and W. G. Sloof, *Acta Materialia* **60**, 2012 (2973).
4. E. M. Bellhouse and J. R. McDermid, *Metallurgical and Materials Transactions A* **42**, 2011 (2753).
5. V. A. Lashgari, C. Kwakernaak and W. G. Sloof, *Oxidation of Metals* **81**, 2014 (435).
6. V. A. Lashgari, G. Zimbitas, C. Kwakernaak and W. G. Sloof, *Oxidation of Metals* **82**, 2014 (249).
7. Y. Suzuki, T. Yamashita, Y. Sugimoto, S. Fujita and S. Yamaguchi, *ISIJ International* **49**, 2009 (564).
8. L. Cho, G. S. Jung and B. C. De Cooman, *Metallurgical and Materials Transactions A* **45**, 2014 (5158).
9. Y. F. Gong, H. S. Kim and B. C. De Cooman, *ISIJ International* **49**, 2009 (557).

10. S. Swaminathan and M. Spiegel, *Surface and Interface Analysis* **40**, 2008 (268).
11. S. Swaminathan and M. Spiegel, *Applied Surface Science* **253**, 2007 (4607).
12. B. D. Cullity and S. R. Stock, *Elements of X-ray Diffraction*, 3rd ed. (Prentice Hall, New York, 2001).
13. C. Bale, P. Chartrand, S. A. Degterov, G. Eriksson, K. Hack, R. Ben Mahfoud, J. Melancon, A. D. Pelton and S. Petersen, *Calphad* **26**, 2002 (189).
14. Y. F. Gong and B. C. De Cooman, *Steel Research International* **82**, 2011 (1310).
15. Factsage Database Documentation, <http://www.crct.polymtl.ca/fact/documentation/>.
16. P. Franke and R. Dieckmann, *Journal of Physics and Chemistry of Solids* **51**, 1990 (49).
17. V. A. Lashgari, *Internal and External Oxidation of Manganese in Advanced High Strength Steels*, Ph.D. thesis, (Delft University of Technology, 2014).
18. W. Mao and W. G. Sloof, *Scripta Materialia* **135**, 2017 (29).
19. K. E. Sickafus, J. M. Wills and N. W. Grimes, *Journal of the American Ceramic Society* **82**, 1999 (3279).
20. N. Sakai, T. Horita, Y. P. Xiong, K. Yamaji, H. Kishimoto, M. E. Brito, H. Yokokawa and T. Maruyama, *Solid State Ionics* **176**, 2005 (681).
21. D. Huin, P. Flauder and J. B. Leblond, *Oxidation of Metals* **64**, 2005 (131).